Late Quaternary active faulting on the inherited Baoertu basement fault within the eastern Tian Shan: Implications for regional tectonic deformation and slip partitioning, NW China

Chuanyong Wu[1,2], Guangxue Ren[3], Siyu Wang[4], Xue Yang[1,2], Gan Chen[1,2], Lei Duan[1,2], Zhuqi Zhang[3], Wenjun Zheng[1,2], Chuanyou Li[3], Zhikun Ren[3], Qiyun Lei[5], Dongli Zhang[1,2]

1. Guangdong Provincial Key Laboratory of Geodynamics and Geohazards, School of Earth Sciences and Engineering, Sun Yat-sen University, Guangzhou, China;

2. Southern Marine Science and Engineering Guangdong Laboratory (Zhuhai), Zhuhai, China;

3. State Key Laboratory of Earthquake Dynamics, Institute of Geology, China Earthquake Administration, Beijing, China;

4. School of Earth and Ocean Sciences, University of Victoria, Victoria, Canada;

5. Earthquake Agency of Ningxia Hui Autonomous Region, Yinchuan, China.

Abstract: The deformation pattern and slip partitioning related to oblique underthrusting of the Tarim Basin in the eastern Tian Shan are not well understood because of the lack of interior deformation images. The Baoertu fault (BF) is an E-W-striking, ~350 km-long reactivated basement structure within the eastern Tian Shan. In this study, we quantify its late Quaternary activity based on detailed high-resolution remote sensing image interpretations and field investigations. Three field observation sites along an ~80 km-long fault segment indicate that the BF is characterized by sinistral thrust faulting. Based on surveying of the displaced geomorphic surfaces with an unmanned drone and dating of the late Quaternary sediments using radiocarbon and optically stimulated luminescence (OSL) methods, we estimate a late Quaternary left-lateral strike-slip rate of 1.87 ± 0.29 mm/yr and a

N-S shortening rate of 0.26 ± 0.04 mm/yr for this fault. The lithospheric BF acts as a decoupling zone and accommodates the left-lateral shearing caused by the oblique underthrusting of the Tarim block. In the eastern Tian Shan, the oblique convergence is partitioned into thrust faulting across the entire range and sinistral slip faulting on the high-dip basement structure within the orogen. This active faulting pattern in the eastern Tian Shan of sinistral shearing in the center and thrust faulting at both sides can be viewed as giant positive flower structures.

Keywords: Tian Shan; inherited structure; Baoertu fault; sinistral slip faulting; slip partitioning

1. Introduction

The Tian Shan orogenic belt, which was amalgamated from several Paleozoic tectonic blocks and sutures (e.g., *Burtman, 1975; Windley et al., 1990*), has been reactivated in response to the ongoing India-Eurasia collision in the late Cenozoic (*Molnar and Tapponnier, 1975; Tapponnier and Molnar, 1979; Avouac et al., 1993; Hendrix et al., 1994*). Its active deformation has been documented by widespread active faulting (*Avouac et al., 1993; Burchfiel et al., 1999; Deng et al., 2000; Thompson et al., 2002*), frequent large earthquakes (Figure 1A) and present-day geodetic measurements (e.g., *Abdrakhmatov et al., 1996; Yang et al., 2008; Zubovich et al., 2010; Wang and Shen, 2020*). Strong uplifted topography with an average elevation greater than 3500 m above sea level (*Deng et al., 2000*), 55-65 km crustal thickness (*Zhao et al., 2003*), ~200 km of north-south (N-S) crustal shortening (e.g., *Avouac et al., 1993*) and ~20 mm/yr current convergence (e.g., *Abdrakhmatov et al., 1996; Yang et al., 2008; Zubovich et al., 2010*) all indicate that Cenozoic deformation of the Tian Shan is mainly dominated by N-S compression. However, GPS measurements reveal that the oblique underthrusting of the Tarim Basin would result in obvious left-lateral shearing in addition to N-S compression in the Tian Shan region (e.g.,

42 *Zubovich et al., 2010; Wu et al., 2019*). Several historical large earthquake surface ruptures within
43 the range, such as the 1911 *Ms* 8.2 Kemin (*Bogdanovich et al., 1914*) and the 1914 *Ms* 7.5 Barkol
44 earthquakes (*Deng et al., 2000*) all involved clear left-lateral faulting, which furthermore testify
45 sinistral shearing motion in the Tian Shan.

46 Previous studies mainly focused on the N-S convergence, that is accommodated by thrust
47 faulting and crustal shortening in both the foreland and hinterland (e.g., *Avouac et al., 1993; Yin et*
48 *al., 1998; Burchfiel et al., 1999; Thompson et al., 2002; Campbell et al., 2019*), and right-lateral
49 faulting and block rotation in the northern Tian Shan (*Molnar and Tapponnier, 1975; Tapponnier*
50 *and Molnar, 1979; Avouac and Tapponnier, 1993; Campbell et al., 2013; Rizza et al., 2019*). In
51 contrast, detailed studies focused on left-lateral faulting within the Tian Shan have rarely been
52 reported. Recent studies (e.g., *Selander et al., 2012; Wu et al., 2019*) suggest that the sinistral
53 shearing is accommodated by several east-northeast (ENE) striking structures within the western
54 Tian Shan. However, the faults in the Chinese eastern Tian Shan strike roughly east-west (E-W) or
55 west-northwest (WNW) (Figure 1) and are proposed to be thrust-dominated faulting. The interior
56 deformation in this region was interpreted as overthrusting of the Paleozoic bedrock upon the
57 elongated and rigid intermontane basins (*Allen et al., 1993; Huang et al., 2015; Wang et al., 2020*).
58 Therefore, it is not clear how the obliquity is achieved by continental fold-and-thrust belts, further,
59 the deformation pattern and slip partitioning in the eastern Tian Shan are not well understood at
60 present.

61 Cenozoic deformation of the Tian Shan is controlled by a series of neogenic thrust faults in
62 the foreland and inherited basement structures within the range (*Tapponnier and Molnar, 1979*).
63 Constraining the fault kinematics and slip rates is essential to better understand how the Tian Shan

evolved and deformed. The Baoertu fault (BF), as a segment of the Paleozoic suture zone between the northern Tian Shan (NTS) and southern Tian Shan (STS) (*Allen et al., 1993; He, 2004*), is an E-W-striking fault within the eastern Tian Shan and extends over 350 km from its western end at Bayanbulak Basin to the eastern tip at Kumish Basin (Figure 1B). In the eastern Tian Shan, previous studies have recognized several thrust- and dextral slip-dominated active faults based on deformed geomorphic surfaces (e.g., *Tapponnier and Molnar, 1979; Yin et al., 1998; Lin et al., 2002; Shen et al., 2003; Huang et al., 2015*) and coseismic surface ruptures (*Deng et al., 2000*). The BF has been proposed to have reactivated during the Cenozoic and to exhibit dominantly right-lateral faulting (*Tapponnier and Molnar, 1979; Allen et al., 1993*). However, remote sensing images and focal mechanisms on this fault display possible left-lateral faulting. To date, no credible information about its timing and kinematics has been quantified in detail. Further, the role and implication of the BF in regional deformation and slip partitioning have not yet been well clarified.

In this study, we focus on the kinematics and slip rate of the inherited BF. Detailed interpretations of high-resolution remote sensing images, field investigations, surveying of deformed geomorphic surfaces by drone at key sites, and dating of the late Quaternary sediments using optically stimulated luminescence (OSL) and radiocarbon methods are utilized to quantify the late Quaternary activity of the BF. This study allows us to image the interior deformation of the eastern Tian Shan, which sheds light on the role and implication of the basement BF in regional tectonic deformation and slip partitioning.

2. Tectonic Setting of the Eastern Tian Shan

In the Late Devonian to early Carboniferous, the first Tian Shan orogeny accreted a passive continental margin along the STS suture on the northern side of the Tarim block. The second Paleozoic orogeny accreted an active continental margin at the northern side to the NTS island arc (*Allen et al., 1993*). After general uplift and denudation in the Mesozoic (*Jolivet et al., 2010*), the reactivated Tian Shan has been strongly uplifted and expanded outward since the late Cenozoic (*Avouac et al., 1993; Yin et al., 1998*). The Tian Shan overthrusts upon the rigid Tarim and Junggar blocks (*Avouac et al., 1993; Zhao et al., 2003*) to form typical foreland basins along its southern and northern flanks. Outward propagation of the Tian Shan has resulted in folding and faulting of the Cenozoic sediments to form E-W-striking foreland fold-and-thrust faults (Figure 1A; *Avouac et al., 1993; Yin et al., 1998; Burchfiel et al., 1999; Deng et al., 2000*). Within the Tian Shan, a series of E-W-striking faults bound the intermontane basins and accommodate the N-S convergence through thick-skinned thrust faulting (*Thompson et al., 2002; Campbell et al., 2019*), and several ENE-striking inherited basement faults accommodate the left-lateral shearing related to the oblique underthrusting of the Tarim Basin (*Selander et al., 2012; Wu et al., 2019*).

GPS measurements indicate that ~6-8 mm/yr of N-S convergence is accommodated by active faulting in the eastern Tian Shan (e.g., *Yang et al., 2008*). The foreland structures are the main strain absorption belts (*Avouac et al., 1993; Burchfiel et al., 1999; Yang et al., 2008*). In the southern piedmont, the Beiluntai fault (BLTF) represents part of the boundary between the STS and the Tarim Basin. Since the late Cenozoic, the BLTF has mainly been dominated by southward thrust faulting, with almost no propagation towards the Tarim Basin. Based on deformed alluvial fan surveying and cosmic-ray exposure dating, *Brown et al.* (*1998*) estimated a slip rate of ~2 mm/yr for the BLTF. Along the northern flank of the Tian Shan, the Urumqi foreland thin-skinned

107 nappe structure is composed of 3-4 rows of active folds and thrust faults (*Avouac et al., 1993;*
108 *Deng et al., 2000*). The late Quaternary N-S shortening rate was estimated to be 3-4 mm/yr (e.g.,
109 *Deng et al., 2000; Yang et al., 2008; Lu et al., 2019*). East of Urumqi, the Bogda foreland nappe
110 absorbs ~1-2 mm/yr of N-S convergence by thrust faulting (*Wu et al., 2016*).

111 Within the range, several Cenozoic intermontane basins without obvious internal shortening
112 deformation are developed (Figure 1A), which are commonly interpreted as pre-existing rigid
113 blocks (*Zhang et al., 1984; Allen et al., 1993*). Active faulting can be clearly observed along the
114 margins of these intermontane basins in the form of thrust faulting or strike-slip faulting (*Yin et al.,*
115 *1998; Lin et al., 2002; Shen et al., 2003; Huang et al., 2015*). Along the northern margin of the
116 Yanqi Basin, the Hejing fold-and-thrust fault shows obvious shortening deformation and
117 accommodates ~0.8 mm/yr of N-S convergence (*Huang et al., 2015*). The inherited A-KF, as a
118 southern boundary of the Turpan Basin, expresses clear right-lateral faulting. *Shen et al.* (*2003*)
119 inferred its dextral slip rate to be 1.0-1.4 mm/yr based on the offset of river terraces and age
120 estimation. The dextral KDF displaces the alluvial fans at the southwestern margin of the Yanqi
121 Basin, which generated a dextral thrust event in the 1927 *Ms* 6.7 Hejing earthquake (*Lin et al.,*
122 *2002*). A recent study (*Huang et al., 2015*) defined a strike-slip rate of ~1.4 mm/yr for the KDF
123 based on the surveying of displaced active channels and OSL dating. These WNW-striking dextral
124 slip faults were proposed to be the transfer zones accommodating the shortening difference in this
125 region (*Tapponnier and Molnar, 1979; Yin et al., 1998*). The eastern Tian Shan is seismically
126 active with moderate earthquakes throughout history (Figure 1B). Although no earthquake with
127 magnitude greater than 7 has been recorded, paleoearthquake studies (e.g., *Huang et al., 2015*)
128 have revealed abundant evidence of prehistoric large earthquake ruptures in this region.

3. Methods

3.1 High-resolution Image Interpretation, Field Mapping and Offset Measurements

High-resolution remote sensing images were mainly used to interpret deformed geomorphic surfaces and fault traces, which allowed us to describe the geometry, kinematics and offsets along the fault. In this study, we mainly utilized images derived from Google Earth to analyze and quantify large-scale fault deformation. For some key sites, we interpreted high-resolution structure-from-motion (SfM) models surveyed by an unmanned drone to better demonstrate the deformed geomorphic surfaces. Before acquiring photographs at the key sites, 6-9 ground control points (GCPs) that consist of 50 cm square red and white papers were evenly distributed in the field. The location of each GCP was surveyed using differential GPS to define a horizontal error of 2 cm and a vertical error of 4 cm. The flight altitude of the unmanned drone was set in the 120-180 m range based on the topographic relief, and the images were processed with the Agisoft Photoscan Pro software. Our detailed techniques and data processing followed those reported by *Snavely et al.* (*2008*). After image correction through the GCPs, we obtained high-resolution digital elevation models (DEMs) (<0.5 m/pixel) using Photoscan from a relative to absolute coordinate system. Finally, we created the hill shade images with the ArcMap software.

We interpreted the images to obtain the fault trace and geometry and divided the displaced river terraces into different grades based on their height and superposition to assess the fault kinematics. In field investigations, we confirmed and modified our interpretations and mapped the deformed surfaces at key sites. From the high-resolution DEMs surveyed by the unmanned drone, we could measure the vertical displacements of the BF by fitting the planar geomorphic markers

150 such as alluvial fans and terraces above and below the scarps. For the strike-slip offsets, some
151 linear markers including terrace risers (*Cowgill, 2007*) and active channels across the BF were
152 utilized to estimate the fault horizontal offsets.

153 **3.2 Late Quaternary Dating**

154 Dating the late Quaternary sediments and geomorphic surfaces is key to quantifying the fault
155 kinematics. Along the E-W-striking BF, several rivers and valleys are present (Figure 2), in which
156 plentiful water resources lead to dense vegetation. Therefore, we found some organic materials in
157 the sediments for radiocarbon dating. In addition, a silty interlayer in the terrace gravels can be
158 sampled for OSL dating.

159 3.2.1 Radiocarbon dating

160 In the field, several gray-black organic sediments and charcoals were found in the sediments
161 of the displaced geomorphic surfaces, which were collected using a knife and packed in plastic
162 sample bags. Our samples were subjected to accelerator mass spectrometry (AMS) radiocarbon
163 dating in the Beta Analytic laboratory. The quoted radiocarbon age calculations used the Libby
164 half-life of 5568 years, and the uncertainties of these ages are reported as 2-sigma. The final
165 results were calibrated using the 2013 INTCAL program (*Reimer et al., 2013*).

166 3.2.2 OSL dating

167 In arid and semiarid areas, OSL is a useful method for dating late Quaternary sediments
168 (*Aitken, 1998; Lu et al., 2007*). In the field, our OSL sample was taken using a steel tube ~20 cm
169 long that was hammered into the silty interlayer. OSL sample preparation and analysis were

performed at the Institute of Disaster Prevention, CEA. The sample was processed under subdued red light. All grain-size fractions were pretreated with 30% H_2O_2 and 10% HCl to remove organic materials and carbonates, respectively. Then, the fine-grain fraction (4-11 μm) was separated using Stokes' law. The polymineralic fine silt grains were immersed in hydrofluosilicic acid (40%) in a centrifuge tube for five days to isolate the quartz. The fine quartz grains were mounted on 9.7-mm steel discs from suspension in acetone. The purity of the quartz was checked by infrared (IR) stimulation and verified through observation of the background IR signal and the typical 110° thermoluminescence (TL) peak.

The equivalent doses of the fine-grained quartz fractions (4-11 μm) were measured using the simplified multiple aliquot regenerative-dose (SMAR) protocol (*Lu et al., 2007*), mainly for experimental convenience. More than three aliquots were measured to determine the natural OSL intensity, and five aliquots were measured to construct a dose-response curve that bracketed the natural OSL intensity. De values were calculated using the sum of the photons detected in the first 1 s of stimulation minus the average of the last 10 s (background) of the OSL luminescence decay curve. An OSL growth curve was constructed using the corrected OSL signal (regenerated dose response (Li)/test dose response (Ti)) and fitting a linear or exponential function to the data to estimate De. The environmental dose rate was determined based on the conversion relation between the dose rate of quartz and the contents of U, Th, and K (*Aitken, 1998*). The calculation of the environmental dose rates of the samples also included the effects of sample water content and a contribution from cosmic rays (*Prescott and Hutton, 1994*). Finally, OSL dates were calculated for each sample using a single average value of the acquired De and the environmental dose rate.

3.2 Trench Excavation

Although no large earthquake has been recorded in history, our field investigations found fresh surface ruptures along the fault. We manually excavated one trench to reveal the fault kinematics and rupture features. We trimmed the trench wall as flat as possible so that the layer units and fault trace in the trench could be easily distinguished. In the field, we utilized printed trench imagery to draft stratigraphic logs and fault interpretations. Radiocarbon samples taken from the trench were analyzed to date the trench stratigraphy and fault activity.

4. Observations and Results

4.1 Fault Geometry, Geomorphology and Offsets

Our study and field investigations mainly focus on an ~80 km-long segment of the BF. In this section, we describe in detail three field observation sites named Site 1 to Site 3 from east to west (Figure 2) and report the fault geomorphology and kinematics.

Site 1: The BF controls the northern margin of the Kumish Basin. Along the fault, clear sinistral slip and southward thrust faulting can be widely observed on late Quaternary geomorphic surfaces (*Ren et al., 2019*). At the NW margin of the Kumishi Basin, the Benbutu River flows from north to south. Along this river valley, four levels of terraces can be identified based on their heights above the riverbed (Figures 3A and 3B). These terraces are mainly developed on the east bank of the river. The T_2 and T_4 terraces, with flat and wide terrace treads, have been left-laterally displaced by the BF. The left-lateral strike-slip offset of the BF is approximately 112.7 m recorded by the T_4 terrace riser (Figure 3C), implying that the BF is dominated by strike-slip faulting. The fault surface exposed by the displaced T_4 terrace shows a gradual increase in the slope from west to east caused by erosion along the fault strike (Figure 3D), indicating that the BF has experienced

213 continuous activity during the late Quaternary.

214 Westward into the range, the fault trace shows a clear linear expression. A series of active
215 channels and ridges that trend roughly N-S or NNW have been left-laterally offset across the fault.
216 The maximum left-lateral offset of these active channels can reach ~4.2-4.4 km (Figure 4). The
217 vertical displacement of geomorphic markers is much smaller than its horizontal offsets (Figure 4),
218 indicating that the BF is mainly characterized by sinistral slip faulting with a small vertical motion
219 component.

220 ***Site 2***: Along the roughly E-W-trending Kerguti River, a tributary of the Qingshui River, the
221 BF shows strong activity because the late Quaternary sediments and river terraces have been
222 faulted. We used remote sensing images derived from Google Earth and field investigations to
223 characterize the geometry and kinematics of the fault. On the north bank of the Kerguti River, a
224 N-facing scarp with south-side-up extends approximately 10 km and left-laterally displaces the
225 active channels and bedrock ridges (Figure 5A). The displaced channels and bedrock ridges and
226 the fault valley clearly mark the traces of the fault and preserve the evidence of long-term
227 left-lateral displacement. At the western end of the N-facing scarp, the fault trace can be clearly
228 identified from several left-laterally displaced channels. A steep active drainage channel (C1)
229 incised into the Paleozoic bedrock has been left-laterally displaced with ~80 m of horizontal
230 displacement. Approximately 100 m to the east, a smaller drainage channel with an incised depth
231 of ~1-2 m records only an ~18 m sinistral slip offset (Figure 5B), which testifies to the later
232 Quaternary activity of the BF.

233 ***Site 3***: Despite the clear linear traces, the fault geometry and kinematics exposed at the

surface appear to show along-strike variations. Between Site 2 and Site 3, the BF presents an ~4 km-wide stepover in its geometry and exhibits obvious differences in kinematics. Near the westernmost part of the E-W-trending Kerguti River valley, a fresh surface rupture is observed. The S-facing fresh scarp of the south-side-down strikes approximately N85°E and is approximately 7 km long. The fault scarp crosses roughly N-S-trending channels and ridges from ~2800 m in the valley in the east to ~3700 m in the range topography at its western end (Figure 6A). The Paleozoic bedrock ridges that can be interpreted as linear markers record a cumulative left-lateral offset of more than 70 m (Figures 6B and 6C). The fresh scarp shows continuous surface traces and dips steeply south (approximately 70°S) (Figures 6B, 6D and 6E). Vertical and left-lateral offsets of a series of active channels and adjacent ridges result in ponding of drainage against the upthrown southern side (Figure 6B). Some pondings of channel thalwegs against the abandoned channels on the north wall of the BF show several meters of left-lateral offsets (Figure 6F).

The scarp height exhibits obvious variations on different geomorphic surfaces, which indicates that the scarp should accumulate from multiple paleoearthquake ruptures (Figure 6B). At the site of N42°35'30", E86°35'50", three grades of terraces can be identified along the NNE-trending river valley, which have been displaced by the BF (Figures 7A and 7B). The high-resolution SfM model provides a detailed image of the fault trace and deformed geomorphic surfaces. Scarp profiles show that the vertical displacements of the fault are ~21.9 m, 8.5 m and 0.7 m high on the T_3, T_2 and T_1 terraces, respectively (Figure 7A). The ~0.7 m-high fresh scarp on the T_1 terrace, which is approximately 1.6 m above the riverbed on the upthrown block of the fault, may represent the latest coseismic vertical displacement. We collected one fine sand sample from

256 the T_1 terrace sediments at a depth of ~35 cm (Figure 7C) for OSL dating. The analytical result of
257 1.19 ± 0.20 ka within the 1σ uncertainty (Table 1) restricts the maximum age for the latest
258 paleoearthquake event.

259 At the site of N42°35'30", E86°36'38", two levels of alluvial terraces that are developed
260 along a NNE-trending river valley ~20-25 m wide (Figure 8A) can be viewed as markers to
261 estimate the fault displacements. The T_1 terrace is approximately 10 m above the riverbed, and the
262 T_2 terrace, which is mainly developed on the east bank of the river, is approximately 15 m above
263 the riverbed. The two levels of terraces have clearly been displaced across the fault. The terrace
264 surface is mostly flat; therefore, we can well constrain the vertical displacements of ~4.5 m and
265 ~3.6 m on the T_2 and T_1 terraces, respectively, based on the high-resolution DEM (Figure 8A).
266 The T_1 terrace riser on the west bank of the river, which shows a steep slope on both walls of the
267 fault and is well preserved, has been left-laterally faulted by 11.9 ± 1.0 m (Figures 8A and 8B). In
268 contrast, the T_1 riser has been laterally eroded on the east bank (Figure 8C).

269 Although the main scarp is mostly concentrated on a single bedding plane and dominated by
270 sinistral slip faulting, a N-facing secondary scarp strikes approximately N55-60°W and extends
271 ~1.2 km to the easternmost extent of the main scarp (Figures 6A and 8A). The N-facing fault scarp
272 displaces the alluvial terraces and fans (Figure 8D). A natural outcrop shows that the secondary
273 scarp is characterized by thrust faulting with dip angles of ~30-40° (Figure 8E). A maximum
274 vertical displacement of ~6.8 m (Figure 8A) is measured on the T_2 terrace. We propose that the
275 N-facing scarp is a bedding moment thrust resulting from compressive stresses in the concave
276 region, similar to that of the 1980 El Asnam rupture (*Philip and Meghraoui, 1983*).

4.2. Fault Kinematics as Revealed by Trench

As described above, the BF is dominated by left-lateral faulting with vertical displacement components. Across the fault scarp on the T_1 terrace at the site of N42°35'30", E86°36'38", we excavated a trench to investigate the late Quaternary activity on the BF. Sediments exposed in the trench are composed of a thick package of terrace gravels in the footwall and aggradations from the scarp front in the hanging wall (Figure 9A). The sedimentary layers in the trench are as follows: U1 is a brown soil layer with small gravel clasts, in which dark-gray charcoal and organic sediment are present. It is 15-20 cm thick on the footwall and ~1.5 m thick on the hanging wall. U2 is terrace sediments consisting of gray alluvial gravels with horizontal bedding, in which gravel clasts are subrounded and poorly sorted with a maximum boulder size of ~80 cm, and some sand lenses can be found. U3 and U5 are interpreted as alluvial wedges in which cobbles and pebbles are mixed with sands. U4 is a brownish-yellow, relatively indistinct mixture (Figure 9B), in which the cobbles and pebbles are mixed with coarse sands derived from the upthrown block that has been pushed approximately 3.6 m high. U6 is a brownish loess layer, which is loose and contains some small dark-gray charcoals.

The trench reveals a normal fault, which is clearly marked by a sheared zone with pebble lineations that is 0.7-0.8 m wide at the trench bottom and only 0.05-0.1 m wide near the surface. The fault dips 60-70° to the south and offsets the terrace gravel layers. The tip of the fault zone seems to rupture the surface sand blanketing the alluvial sediments (Figure 9C). The vertical displacement of the fault is approximately 0.4 m if we take the base of U1 as a marker (Figure 9C), which should represent the coseismic displacement of the last paleoearthquake. The vertical displacement on the T_1 terrace across the fault is approximately ~3.6 m (Figure 8A), which, we

believe, represents the cumulative vertical displacement of multiple paleoseismic events. On the wall of the trench, U3 and U5 are all wedge-shaped and show indistinct mixture without bedding, these characteristics might represent colluvial deposits formed after a vertical-faulting earthquake. We therefore suggest that there were at least another two surface rupturing events have occurred on the BF after T_1 was abandoned.

In this trench, we collected five radiocarbon samples (Figure 9A). The analytical results are summarized in Table 2. The radiocarbon sample HS-04, which was collected from the fine sand interlayer of T_1 sediments (Figure 9A), yields a depositional age of 6892-6730 cal yr BP (Table 2) for the T_1 terrace. HS-05, HS-06 and HS-07 were collected in the U1 layer overlying the terrace, that constrained the minimum abandonment age of the T_1 terrace. The sample HS-03, which was collected in U6, however, shows a younger age than the upper samples. The charcoal sample HS-03 is near a hole and may be contaminated. Therefore, we suggest that the result for HS-03 is not credible.

5. Discussion and Implications

5.1 Evidence of Left-lateral Strike-slip Faulting and Slip Rate of the BF

Previous studies (e.g., *Tapponnier and Molnar, 1979; Yin et al., 1998; Lin et al., 2002; Huang et al., 2015*) recognized several WNW-striking dextral slip faults named the Kuruk Tagh fault system in the eastern Tian Shan. The inherited BF was considered a branch fault of the Kuruk Tagh fault system that was dominated by right-lateral faulting during the late Cenozoic (*Tapponnier and Molnar, 1979*). However, our field investigations and detailed interpretations of high-resolution images indicate that the overall sense of motion of the BF exhibits clear left-lateral

faulting. Along the fault, a series of left-laterally displaced late Quaternary terraces (Figures 6, 7 and 8) imply its kinematics, and some linear markers of left-laterally displaced active channels (Figure 4) verify its long-term sinistral slip faulting. Furthermore, the focal mechanism of the 1995 *Ms* 5.0 earthquake that occurred on the BF (Figure 1B) also indicates that the fault is mainly characterized by left-lateral faulting. In the field, the fresh rupture plane and fault outcrop at Site 3 reveal that the BF has undergone obvious south-dipping normal faulting. Along the fault, the grayish-green Devonian bedrock dipping south at ~70° can be observed at the surface, which agrees with the fault plane. A deep structure profile indicates that the BF dips north and thrusts southward (*Shao et al., 1996*). The fault plane inferred from the focal mechanism to dip NNW at a dip angle of 65°. We infer that the normal faulting component observed at the surface may be caused by the steep fault dip at the subsurface, which follows Paleozoic rock bedding and yields a south-dipping normal fault. The fault kinematics may have depth-dependent variations caused by stratigraphy or landforms, which has been reported on the surface ruptures of the 1980 El Asnam earthquake (*Philip and Meghraoui, 1983*) and the 2008 Wenchuan earthquake (*Liu-Zeng et al., 2010*). Therefore, the activity of the BF is dominated by left-lateral thrust faulting.

The minor surface erosion and distinct presence of deformed landscapes in our study area allows us to quantify the fault slip rate. Calculating strike-slip rates based on displaced fluvial terraces heavily relies on the reconstruction of offset landforms (e.g., *Cowgill, 2007; Zhang et al., 2007*). In the case of alluvial terraces that are offset far from active channels, the terraces on the upstream side of the fault can protect the risers downstream from lateral erosion (*Zhang et al., 2007*). Therefore, the abandonment age of the upper terrace or the depositional age of the lower terrace should be close to the time at which the displacement of the terrace riser initiated

(*Zhang et al., 2007*). At the site of N42°35'30", E86°36'38", we quantified a left-lateral offset of 11.9 ± 1.0 m for the T_1 terrace riser on the west bank of the stream. The T_1 on the downstream west bank has been protected by topography on the upstream side of the fault. In contrast, the T_1 terrace on the east bank has been laterally eroded (Figures 8A and 8C). Therefore, we utilize the sinistral offset of the T_1 terrace riser on the west bank and the abandonment age of T_1 to estimate the strike-slip rate along the fault. Our radiocarbon dating results yield a minimum T_1 abandonment age of 6263-6001 cal yr BP from HS-05 and a depositional age of 6892-6730 cal yr BP from HS-04 (Table 2). Thus, we can define the terrace abandonment age of T_1 to be 6892-6001 cal yr BP and obtain a sinistral slip rate of 1.87 ± 0.29 mm/yr for the BF. On the T_1 terrace, we measured a vertical displacement of 3.6 ± 0.3 m (Figure 8A). The fault dip angle revealed by our trench is 60-70° at the surface and approximately 65° at depth inferred from the focal mechanism. Therefore, we can roughly calculate the shortening value as 1.54-1.82 m based on a simple trigonometric function relation $s = d/\tan\theta$, where s represents the crustal shortening value (unit: m), d represents the vertical height of the scarp (unit: m) and θ represents the fault dip angle. Thus, we can obtain a shortening rate of 0.26 ± 0.04 mm/yr for the BF.

5.2 Large Earthquake Rupturing on the BF

Along the Kerguti River valley, a surface rupture that extends ~7 km and strikes roughly E-W appears very fresh along its entire length. Therefore, we suggest that this fault segment has been reactivated in the recent past, as verified by our OSL dating of OSL-HS-1801 (Table 1).

Different displacements of the displaced geomorphic surfaces along the ~7 km-long fault scarp imply that multiple paleoearthquakes have occurred along this segment. Our trench also

363 reveals three paleoseismic events (Figure 9). The long-term ratio of strike-slip and vertical slip is
364 approximately 3:1, inferred from the accumulated displacements on the T_1 terrace at the site of
365 N42°35'30", E86°36'38". Therefore, based on a maximum vertical displacement of ~0.7 m
366 observed at the site of N42°35'30", E86°35'50", we can roughly estimate the amount of strike-slip
367 movement as ~2.1 m for the latest paleoearthquake. The ratio of oblique slip (~2.2 m) to length
368 (~7 km) on the BF is clearly much larger than those for most earthquakes. Previous studies have
369 reported that the 1992 *Mw* 7.2 Suusamyr earthquake generated surface ruptures less than 4 km
370 long with a slip of ~4.2 m (*Ghose et al., 1997*) and that the 2001 *Mw* 7.6 Bhuj earthquake
371 involved ~10 m slip on a rupture with a length of only ~20 km (*Schmidt and Bürgmann, 2006*).
372 Explanations for the short surface ruptures are that a portion of the subsurface slip was
373 transformed to folding or that the coseismic slip took place at depth. The basement BF cuts deeply,
374 as manifested by the deep structure (*Shao et al., 1996*) and an ~32 km focal depth for the *Ms* 5.0
375 earthquake that occurred on this fault, which is larger than the majority of focal depths of (14 ± 5)
376 km (*Wright et al., 2013*). The focal depth has an important effect on the surface rupture (*Clark et*
377 *al., 2014*). We speculate that the coseismic ruptures have been partly apportioned at depth, which
378 may be caused by their great focal depths. Based on an ~7 km-long surface rupture, a 32 km focal
379 depth and an ~2.2 m slip value, we can estimate a minimum magnitude of *Mw* 6.8 (Mo = 3*e*10×7
380 km×32 km×2.2 m/sin 70) for this fresh rupture. At the northern margin of the Kumish Basin, Ren
381 et al. (*2019*) reported a fresh surface rupture that only extends few kilometers long. Short ruptures
382 on the surface may be a main feature of the BF because of the deep seismic focus. It would
383 underestimate the paleoearthquake magnitude on the basement faults if based on the traditional
384 regression of surface ruptures and moment magnitude.

5.3 Implications of Left-lateral Faulting on the BF for Regional Tectonic Deformation and Slip Partitioning

The E-W-striking BF, as a reactivated Paleozoic suture zone, exhibits clear strike-slip faulting instead of the expected thrust faulting (*Thompson et al., 2002*) or dextral slip faulting (*Tapponnier and Molnar, 1979*). As far as currently known, the BF is the only sinistral slip fault within the eastern Tian Shan. The inherited basement BF with a high dip angle shows continuous surface traces and exhibits clear sinistral strike-slip motions. The long-term strike-slip deformation has mainly concentrated on this fault, as manifested by several kilometer-scale sinistral offsets of the channels (Figure 4). The BF accommodates the permanent left-lateral offsets caused by oblique underthrusting of the Tarim through intermittent large earthquake rupturing. Therefore, the active deformation in the eastern Tian Shan composes interior sinistral thrust shearing and foreland reverse faulting (*Zubovich et al., 2010; Wu et al., 2019*). From the geodetic data of *Wang and Shen* (*2020*), we can identify sinistral shearing within the eastern Tian Shan region. GPS profile across the eastern Tian Shan reveals ~1.5 mm/yr sinistral motion (Figure 10), which matches our geological strike-slip rate of 1.87 ± 0.29 mm/yr well, indicating the fault-parallel convergence is completely accommodated by the upper block strike-slip fault (*Bardley et al., 2017*).

The active deformation is widely distributed across the “soft” and “hot” lithospheric block of the entire Tian Shan orogenic belt (*Thompson et al., 2002; Zubovich et al., 2010; England and Molnar, 2015*). The most fault planes dip gently and extend in a depth of brittle upper crust (*Ghose et al., 1997*). Slip partitioning is usually envisioned as resulting from a local frictional balance between the megathrust and the overriding block strike-slip fault (*McCaffrey, 1991*). The

low-angle ductile thrust sheets accommodate large shortening strains, however, that cannot accommodate the oblique convergence. The inherited basement BF displays obvious sinistral faulting despite in a stress field of favoring thrust faulting, which may be caused by the pre-existing weak zone and low friction of fault plane (*Henyey and Wasserburg, 1971; Webb and Johnson, 2006*). The sinistral shear zone rooting into a deep crustal low-angle detachment, marks the point at which oblique convergence is partitioned into separate strike-slip and reverse faulting (*Holdsworth and Strachan, 1991; Allen et al., 2017*). This pattern of slip partitioning can be generally observed in the oblique plate subduction zones (*Allen et al., 2017*).

The shortening rate of 0.26 ± 0.04 mm/yr of the BF indicates that this fault absorbs only minor amounts of N-S convergence. The more important role of the BF seems to act as a nucleation zone, which can cause deformation in deep to propagate upwards as a partitioned system of reverse and obliquely slipping faults (*Bowman et al., 2003; Selander et al., 2012; Heron et al., 2019*). This suite of active faults in the eastern Tian Shan with a sinistral slip fault in the center and thrust faults on both sides can be viewed as giant crustal-scale positive flower structures (Figure 11). As a kinematic decoupling zone from the deep ductile deformation to the shallow brittle deformation, the reactivated pre-existing basement structure strongly influences tectonic localization, deformation architecture and the pattern of continental mountain building (*Sokoutis and Willingshofer, 2011; Jourdon et al., 2017*).

6. Conclusions

The E-W-striking Baoertu fault within the eastern Tian Shan extends ~350 km in length. On remote sensing images, this basement fault exhibits a clear linear expression. The displaced late

Quaternary geomorphic surfaces, active channels, and fresh ruptures along the fault attest to its strong activity during the late Quaternary. Detailed interpretations of high-resolution remote sensing images, field observations and mapping reveal that the Baoertu fault is a sinistral thrust fault zone. Based on surveying of the deformed geomorphic surfaces through an unmanned drone and geochronological dating using radiocarbon and OSL methods, we obtain a sinistral slip rate of 1.87 ± 0.29 mm/yr and a N-S shortening rate of 0.26 ± 0.04 mm/yr for the fault. Our field investigations reveal a young paleoearthquake event that occurred after 1.19 ± 0.20 ka.

The Baoertu fault, as a reactivated Paleozoic suture zone between the northern Tian Shan and southern Tian Shan, accommodates the left-lateral shearing caused by the oblique northward penetration of the Tarim block. This basement fault acts as a nucleation zone for slip partitioning in the eastern Tian Shan. The oblique convergence is partitioned into thrust faulting across the entire range and sinistral slip faulting within the orogen. This suite of active faults in the eastern Tian Shan with the sinistral slip fault in the center and thrust faults at both sides can be viewed as a set of crustal-scale giant positive flower structures. The reactivated basement structure has important influence on the deformation pattern and slip partitioning associated with continental mountain building.

Acknowledgments: This research is supported by the Second Tibetan Plateau Scientific Expedition and Research Program (STEP) (2019QZKK0901), the National Nonprofit Research Grant of China (IGCEA1607) and the National Science Foundation of China (41672208 and 41590861). Many thanks are due to the Institute of Disaster Prevention, CEA, and Beta Analytic laboratory for their support with sample dating. Partial high-resolution remote sensing images were obtained from Google Earth. The GPS data (Table S1) is available through Wang and Shen

(2020). The details of measurement and age calculation of the radiocarbon samples are available online (https://figshare.com/s/b2331d3b08dc5929c2ad).

References

Abdrakhmatov, K.Y., Aldazhanov, S.A., Hager, B. H., Hamburger, M.W., Herring, T.A., & Kalabaev, K.B. (1996). Relatively recent construction of the Tian Shan inferred from GPS measurements of present-day crustal deformation rates. Nature 384 (6608), 450-453. http://doi.org/10.1038/384450a0

Aitken, M.J. (1998). An introduction to optical dating: The dating of quaternary sediments by the use of photon-stimulated luminescence. New York: Oxford University Press.

Allen, M.B., Walters, R. J., Song, S., Saville, C., DePaola, N., Ford, J., Hu, Z., & Sun, W. (2017). Partitioning of oblique convergence coupled to the fault locking behavior of fold-and-thrust belts: Evidence from the Qilian Shan, northeastern Tibetan Plateau. *Tectonics*, 36, 1679-1698. https://doi.org/10.1002/2017TC004476

Allen, M.B., Windley, B.F., Zhang, C., & Guo, J. (1993). Evolution of the Turfan Basin, Chines central Asia. Tectonics, 12(4), 889-896. http://doi.org/0278-7407/93/93TC-00598

Avouac, J.P., & Tapponnier, P. (199)3. Kinematic model of active deformation in Central Asia. *Geophys. Rese. Lett.* 20 (10), 895-898. http://doi.org/10.1029/93GL00128

Avouac, J.P., Tapponnier, P., Bai, M.X., You, H.C., & Wang, G. (1993). Active faulting and folding in the northern Tian Shan and rotation of Tarim relative to Dzungarian and Kazakhstan. *J. Geophys. Res.* 98, 6755-6804. http://doi.org/10.1029/92JB01963

Bogdanovich, K.I., Kark, I.M., Korolkov, B.Y., & Mushketov, D.I. (1914). Earthquake in northern district of Tien Shan, 22 December 1911 (4 January 1911), paper presented at Geology Committee, New series, 89, St.

Petersburg (in Russian, extended abstract in Frence).

Bowman, D., King, G., & Tapponnier, P. (2003). Slip partitioning by elastoplastic propagation of oblique slip at depth. Science, 300(5622), 1121-1123. https://doi.org/10.1126/science.1082180

Bradley, K.E., Feng, L., Hill, E.M., Natawidjaja, D.H, & Sieh, K. (2017). Implications of the diffuse deformation of the Indian Ocean lithosphere for slip partitioning of oblique plate convergence in Sumatra. J. *Geophys. Res. Solid Earth*, 122, 572-591. https://doi.org/10.1002/2016JB013549

Brown, E.T., Bourles, D.L., Burchfiel, B.C., Deng, Q.D., Li, J., Molnar, P., Raisbeck, G.M., & Yiou, F. (1998). Estimation of slip rates in the southern Tien Shan using cosmic ray exposure dates of abandoned alluvial fans. *Geol. Soc. Am. Bull.* 110 (3), 377-386. http://doi.org/10.1130/0016-7606(1998)110<0377:EOSRIT>2.3.CO;2

Burchfiel, B., Brown, E.T., Deng, Q.D., Feng, X.Y., Li, J., Molnar, P., Shi, J.B., Wu, Z.M., & You, H.C. (1999). Crustal shortening on the margins of the Tien Shan, Xinjiang, China. *Int. Geology. Rev.* 41 (8), 665-700.

Burtman, V.S. (1975). Structural geology of the Variscan Tien Shan. *Amer. J. Sci.* 280, 725-744.

Campbell, G.E., Walker, R.T., Abdrakhmatov, K., Carolin, S., Carr, A.S., Elliott, J.R., Jackson, J., Mackenzie, D., Rizza, M., & Rodes, A. (2019). Rapid late-Quaternary slip, repeated prehistoric earthquake rupture, and widespread landsliding associated with the Karakudzhur Thrust, central Kyrgyz Tien Shan. Tectonics, 38 (11), 3740-3764. http://doi.org/10.1029/2018TC005433

Campbell, G.E., Walker, R.T., Abdrakhmatov, K., Schwenninger, J.L., Jackson, J., Elliott, J.R., & Copley, A. (2013). The Dzhungarian fault: Late Quaternary tectonics and slip rate of a major right-lateral strike-slip fault in the northern Tien Shan region. *J. Geophys. Res. Solid Earth*, 118, 5681-5698.

http://doi.org/10.1002/jgrb.50367

Clark, D., McPherson, A., Allen, T., & DeKool, M. (2014). Coseismic surface deformation caused by the 23 March 2012 *Mw* 5.4 Ernabella (Pukatja) earthquake, Central Australia: Implications for fault scaling relations in cratonic settings. *Geol. Soc. Am. Bull.* 104 (1), 24-39. http://doi.org/10.1785/0120120361

Cowgill, E. (2007). Impact of riser reconstructions on estimation of secular variation in rates of strike-slip faulting: Revisiting the Cherchen River site along the Altyn Tagh fault, NW China. *Earth Planet. Sci. Lett.* 254 (3-4), 239-255. http://doi.org/10.1016/j.epsl.2006.09.015

Deng, Q.D., Feng, X.Y., Zhang, P.Z., Xu, X.W., Peng, S.Z., & Li, J. (2000). Active Tectonics of Tianshan. Seismological Press, Beijing (in Chinese).

England, P., & Molnar, P. (2005). Late Quaternary to decadal velocity fields in Asia. *J. Geophys. Res.* 110, B12401, http://doi.org/10.1029/2004JB003541

Ghose, S., Mellor, R.J., Korjenkov, A.M., Hamburger, M.W., Pavlis, T.L., Pavlis, G.L., Omuraliev, M., Mamyrov, E., & Muraliev, A.R. (1997). The *Ms*=7.3 1992 Suusamyr, Kyrgyzstan, earthquake in the Tien Shan: 2. Aftershock focal mechanisms and surface deformation. *Bull. Seismol. Soc. Am.* 87 (1), 23-38. http://doi.org/10.1029/96JB01781

He, G.Q. (2004). Tectonic map (1:2500000) of Xinjiang and its adjacent areas, China. Beijing: Geological Publishing House.

Hendrix, M.S., Dumitrn, T.A., & Graham, S.A. (1994). Late Oligocene-Early Miocene unroofing in the Chinese Tianshan: An early effect of the India-Asia collision. *Geology* 22 (6), 487-490. http://doi.org/10.1130/0091-7613(1994)022<0487:LOEMUI>2.3.CO;2

Henyey, T.L., & Wasserburg, G.J. (1971). Heat flow near major strike-slip faults in California. *J. Geophys. Res.*, 76 (32), 7924-7946. https://doi.org/10.1029/JB076i032p07924

Heron, P.J., Pysklywec, R.N., Stephenson, R., & van Hunen, J. (2019). Deformation driven by deep and distant structures: Influence of a mantle lithosphere suture in the Ouachita orogeny, southeastern United States. Geology 47 (2), 147-150. https://doi.org/10.1130/G45690.1

Holdsworth, R.E., & Strachan, R.A. (1991). Interlinked system of ductile strike-slip and thrusting formed by Caledonian sinistral transpression in northeastern Greenland. *Geology*, 19, 510-513. https://doi.org/10.1130/0091-7613(1991)019<0510:ISODSS>2.3.CO;2

Huang, W., Yang, X., Li, A., Pierce, I., Thompson, J., Angster, S., & Zhang, L. (2015). Late Pleistocene shortening rate on the northern margin of the Yanqi Basin, southeastern Tian Shan, NW China. *J. Asian Earth Sci.* 112, 11-24. https://doi.org/10.1016/j.jseaes.2015.08.024

Jolivet, M., Dominguez, S., Charreau, J., Chen, Y., Li, Y., & Wang, Q. (2010). Mesozoic and Cenozoic tectonic history of the Central Chinese Tian Shan: Reactivated tectonic structures and active deformation. *Tectonics* 29, TC6019. https://doi.org/10.1029/2010TC002712

Jourdon, A., Le Pourhiet, L., Petit, C., & Rollandet, Y. (2017). The deep structure and reactivation of the Kyrgyz Tien Shan: Modelling the past to better constrain the present. *Tectonophysics* 746, 530-548, https://doi.org/10.1016/j.tecto.2017.07.019

Lin, A., Fu, B.H., Kano, K.I., Maruyama, T., & Guo, J. (2002). Late Quaternary right-lateral displacement along active faults in the Yanqi Basin, southeastern Tian Shan, northwest China. *Tectonophysics* 354, 157-178. https://doi.org/10.1016/s0040-1951(02)00288-3

Liu-Zeng, J., Zhang, Z., Wen, L., Tapponnier, P., Sun, J., Xing, X., Hu, G., Xu, Q., Zeng, L., Ding, L., Ji, C., Hudnut, K.W., & Van der Woerd, J. (2009). Co-seismic ruptures of the 12 May 2008, Ms 8.0 Wenchuan earthquake, Sichuan: East-west crustal shortening on oblique, parallel thrusts along the eastern edge of Tibet. E*arth Planet. Sci. Lett.* 286, 355-370. https://doi.org/10.1016/j.epsl.2009.07.017

Lu, H., Li, B., Wu, D., Zhao, J., Zheng, X., Xiong, J., & Li, Y. (2019). Spatiotemporal patterns of the Late Quaternary deformation across the northern Chinese Tian Shan foreland. *Earth-Sci. Rev.* 194, 19-37. https://doi.org/10.1016/j.earscirev.2019.04.026

Lu, Y.C., Wang, X.L., & Wintle, A.G. (2007). A new OSL chronology for dust accumulation in the last 130, 000 yr for the Chinese Loess Plateau. *Quaternary Res.* 67 (1), 152-160. https://doi.org/10.1016/j.yqres.2006.08.003

McCaffrey, R. (1991). Slip vectors and stretching of the Sumatran fore arc. *Geology*, 19, 881-884.

Molnar, P., & Tapponnier, P. (1975). Cenozoic tectonics of Asia: Effects of a continental collision: Features of recent continental tectonics in Asia can be interpreted as results of the India-Eurasia collision. *Science* 189 (4201), 4l9-426. http://doi.org/10.1126/science.189.4201.419

Philip, H., & Meghraoui, M. (1983). Structural analysis and interpretation of the surface deformations of the El Asnam earthquake of October 10, 1980. *Tectonics* 2, 17-49. http://doi.org/10.1029/tc002i001p00017

Prescott, J.R., & Hutton, J.T. (1994). Cosmic ray contribution to dose rates for luminescence and ESR dating: Large depths and long-term time variations. *Radiat. Meas.* 23 (2-3), 497-500. http://doi.org/10.1016/1350-4487(94)90086-8

Reimer, P.J., Bard, E., Bayliss, A., Beck, J.W., Blackwell, P.G., Ramsey, C.B., et al. (2013). IntCal13 and Marine13 radiocarbon age calibration curves 0-50,000 years cal BP. *Radiocarbon* 55 (4), 1869-1887.

http://doi.org/10.2458/azu-js-rc.55.16947

Ren, G.X., LI, C.Y., Wu, C.Y., Wang, S.Y., Zhang, H.P., Ren, Z.K., Li, X.N. (2019). The late Quaternary activity and formation mechanism of Baoertu fault zone, eastern Tian Shan segment. Seismology and Geology, 41(4), 856-871. http://doi.org/10.3969/j.issn.0253-4967.2019.04.004

Rizza, M., Abdrakhmatov, K., Walker, R., Braucher, R., Guillou, V., Carr, A.S., Campbell, G., McKenzie, D., Jackson, J., Aumaître, G., Bourlès, D.L., & Keddadouche, K. (2019). Rate of slip from multiple Quaternary dating methods and paleoseismic investigations along the Talas-Fergana Fault: tectonic implications for the Tien Shan Range. *Tectonics*, http://doi.org/10.1029/2018TC005188

Schmidt, D.A., & Bürgmann, R. (2006). InSAR constraints on the source parameters of the 2001 Bhuj earthquake. *Geophys. Res. Lett.* 33, L02315, http://doi.org/10.1029/2005GL025109

Selander, J., Oskin, M., Ormukov, C., & Abdrakhmatov, K. (2012). Inherited strike-slip faults as an origin for basement-cored uplifts: Example of the Kungey and Zailiskey ranges, northern Tian Shan. *Tectonics* 31, TC4026, http://doi.org/10.1029/2011TC003002

Shao, X.Z., Zhang, J.R., Fan, H.J., Zheng, J.D., Xu, Y., & Zhang, H.Q. (1996). The crust structures of Tianshan orogenic belt: A deep sounding work by converted waves of earthquakes along Urumqi-Korla profile. *Chinese J. Geophys.* 39 (3), 336-346 (in Chinese).

Shen, J., Yang, Y.P., Li, Y.Z., Jiang, H., & Xiang, Z.Y. (2003). Late Quaternary right-lateral strike-slip faulting along Bolokenu-Aqikekuduk fault in Chinese Tian Shan. *Seismol. Geol.*, 25 (2), 183-19 (in Chinese with English abstract).

Snavely, N., Seitz, S.M., & Szeliski, R. (2008). Modeling the world from internet photo collections. *Int. J. Comput.*

Vision 80 (2), 189-210. http://doi.org/10.1007/s11263-007-0107-3

Sokoutis, D., & Willingshofer, E. (2011). Decoupling during continental collision and intra-plate deformation. *Earth Planet. Sci. Lett.* 305(3-4), 435-444. https://doi.org/10.1016/j.epsl.2011.03.028

Tapponnier, P., & Molnar, P. (1979). Active faulting and Cenozoic tectonics of the Tien Shan, Mongolia, and Baykal regions. *J. Geophys. Res.* 84, 3245-3459, http://doi.org/10.1029/JB084iB07p03425

Thompson, S.C., Weldon, R.J., Rubin, C.M., Abdrakhmatov, K., Molnar, P., & Berger, G.W. (2002). Late quaternary slip rates across the central Tien Shan, kyrgyzstan, central Asia. *J. Geophys. Res.* 107 (B9), 2203, http://doi.org/10.1029/2001JB000596, 2002

Wang, M., & Shen, Z.K. (2020). Present-day crustal deformation of continental China derived from GPS and its tectonic implications. *J. Geophys. Res.*, 125, e2019JB018774. https://doi.org/10.1029/2019JB018774

Wang, S., Jiao, R., Ren, Z., Wu, C., Ren, G., Zhang, H., Lei, Q. (2020). Active thrusting in an intermontane basin: the Kumysh Fault, eastern Tian Shan. Tectonics, https://doi.org/10.1029/2019TC006029

Webb, L.E., & Johnson, C. L. (2006). Tertiary strike-slip faulting in southeastern Mongolia and implications for Asian tectonics. *Earth Planet. Sci. Lett.* 241(1-2), 323-335. https://doi.org/10.1016/j.epsl.2005.10.033

Windley, B.F., Allen, M.B., Zhang, C., Zhao, Z.Y., & Wang, G.R. (1990). Paleozoic accretion and Cenozoic redeformation of the Chinese Tien Shan range, central Asia. *Geology* 18 (2), 128-131. http://doi.org/10.1130/0091-7613(1990)018<0128:PAACRO>2.3.CO;2

Wright, T.J., Elliott, J.R., Wang, H., & Ryder, I. (2013). Earthquake cycle deformation and the Moho: Implications for the rheology of continental lithosphere. *Tectonophysics* 609, 504-523. http://doi.org/10.1016/j.tecto.2013.07.029

590 Wu, C., Zheng, W., Zhang, P., Zhang, Z., Jia, Q., Yu, J., Zhang, H., Yao, Y., Liu, J., Han, G., & Chen, J. (2019).
591 Oblique thrust of the Maidan fault and late Quaternary tectonic deformation in the southwestern Tian Shan,
592 Northwestern China. *Tectonics* 38 (8), 2625-2645. http://doi.org/10.1029/2018TC005248

593 Wu, C.Y., Wu, G.D., Shen, J., Dai, X.Y., Chen, J.B., & Song, H.P. (2016). Late Quaternary tectonic activity and
594 crustal shortening rate of the Bogda mountain area, eastern Tian Shan, China. *J. Asian Earth Sci.*, 119, 20-29,
595 http://doi.org/10.1016/j.jseaes.2016.01.001

596 Yang, S.M., Li, J., & Wang, Q. (2008). The deformation pattern and fault rate in the Tianshan Mountains inferred
597 form GPS observations. *Sci. China Ser. D* 51 (8), 1064-1080 (in Chinese).

598 Yin, A., Nie, S., Craig, P., Harrison, T.M., Ryerson, F.J., Qian, X.L., & Yang, G. (1998). Late Cenozoic tectonic
599 evolution of the southern Chinese Tian Shan. *Tectonics* 17 (1), 1-27, http://doi.org/10.1029/97TC03140

600 Zhang, P.Z., Molnar, P., & Xu, X.W. (2007). Late Quaternary and present-day rates of slip along the Altyn Tagh
601 fault, northern margin of the Tibetan plateau. *Tectonics* 26, TC5010. http://doi.org/10.1029/2006TC002014

602 Zhang, Z.M., Liou, J.G., & Coleman, R.G. (1984). An outline of the plate tectonics of China. *Geol. Soc. Am. Bull.*
603 95 (3), 295-312. https://doi.org/10.1130/0016-7606(1984)95<295:AOOTPT>2.0.CO;2

604 Zhao, J.M., Liu, G.D., Lu, Z.X., Zhang, X., & Zhao, G.Z. (2003). Lithospheric structure and dynamic processes of
605 the Tianshan orogenic belt and the Junggar basin. *Tectonophysics* 376 (3-4), 199-239.
606 http://doi.org/10.1016/j.tecto.2003.07.001

607 Zubovich, A.V., Wang, X.Q., Scherba, Y.G., Schelochkov, G.G., Reilinger, R., Reigber, C., et al. (2010). GPS
608 velocity field for the Tien Shan and surrounding regions. *Tectonics* 29, TC6014,
609 http://doi.org/10.1029/2010TC002772

Captions:

Figure 1 (A) Distribution of active faults and seismicity of magnitude greater than *Ms* 6 (seismic data are from the China Earthquake Networks Center (CENC) and USGS catalogs) in the Tian Shan region. (B) Active faults and seismicity of magnitude greater than *Ms* 5 in the eastern Tian Shan (see Figure 1A for the location; seismic data and focal mechanism of the 1995 *Ms* 5.0 earthquake on the BF are from the CENC catalog). A-KF: Achik-Kuduk fault; KDF: Kaiduhe fault; BLTF: Beiluntai fault.

Figure 2 Digital elevation model with a resolution of 30 m showing a clear linear expression along the fault (red arrows mark the fault trace). A series of active channels of trending roughly N-S (light blue lines represent the rivers and channels) have been left-laterally offset across the BF.

Figure 3 (A and B) High-resolution remote sensing image (derived from Google Earth) and its geomorphic interpretation (dotted box in Figure 3B represents the location of Figure 3C). (C) Restoration of 112.7 ± 4.1 m left-lateral slip realigns the well-defined T_4 terrace riser (the yellow lines represent the upper and lower boundaries of terrace riser) on both sides of the fault. (D) Photograph facing ~W shows an eastward increase in the exposed fault plane.

Figure 4 High-resolution remote sensing image (derived from Google Earth) showing the active channels (blue lines) that have been left-laterally offset across the fault. Left-lateral offsets ranging from ~0.9 km to ~4.4 km can be observed on different scale channels. Topographic profiles show only ~300 m vertical motion across the BF.

Figure 5 (A) High-resolution remote sensing image (derived from Google Earth) showing the left-laterally displaced ridges and active channels that can be viewed as markers of the fault trace on the north bank of the Kerguti River. Red arrows indicate the fault trace, and blue lines represent the left-laterally offset active channels. (B) Photograph facing ~NW shows the left-laterally displaced active channels (see Figure 5A for the location).

Figure 6 (A) High-resolution remote sensing image (derived from Google Earth) showing the distribution and geometry of the fresh ruptures. (B) Digital elevation model (DEM) surveyed by an unmanned drone showing the faulted landscapes along the eastern segment of the fresh ruptures. (C) Photograph facing ~S shows a left-laterally displaced bedrock ridge. (D) Photograph facing ~W shows the faulted landscapes and steep dip fault surface. (E) Photograph facing ~E shows the faulted landscapes and fresh rupture surface. (F) Photograph showing a vertical displacement and significant left-lateral offset. The downstream channel has been abandoned, and the channel thalweg (white line with arrow) on the south wall shows tens of meters of left-lateral offset.

Figure 7 (A) Digital elevation model (DEM) surveyed by an unmanned drone showing the displaced terraces. The counter-slope fault scarps are 21.9 ± 1.6 m on T_3, 8.5 ± 0.6 m on T_2 and 0.7 ± 0.2 m on T_1 (see Figure 6B for the locations). (B) Photograph facing ~E shows the displaced alluvial terraces. (C) Photograph facing ~NE shows the sediments of the T_1 terrace and the sample location for OSL-HS-1801.

Figure 8 (A) Digital elevation model (DEM) surveyed by an unmanned drone showing the fault geometry and displaced terraces. (B) Photograph facing ~W shows the left-lateral offset T_1 terrace riser of 11.9 ± 1.0 m. (C) Photograph facing ~E shows the landscape on the east bank of the river. (D) Photograph facing ~E shows the N-facing vertical scarp on the T_1 and T_2 terraces. (E) Photograph facing ~E shows a thrust fault dipping south at 30-40°.

Figure 9 (A) Trench photograph facing ~E and interpreted section on the T_1 terrace at the site of N42°35'30", E86°36'38" (see Figure 8A for the trench location). (B) Field photograph showing the accretion layer in front of the scarp (see Figure 9A for the location). (C) Field photograph showing the displaced layers near the surface (see Figure 9A for the location). The yellow dotted lines represent the base boundary of U1.

Figure 10 Profile of velocity components normal to structure striking (E-W components) across the eastern Tian

652 Shan (profile from (85.3°, 41.0°) to (85.3°, 45.0°) with a width of 240 km; see Figure 1A for the profile location).

653 GPS data are from *Wang and Shen* (2020), and the red line represents the BF.

654 **Figure 11** Schematic diagram of tectonic deformation in the Chinese eastern Tian Shan (deep structure modified

655 after Zhao et al., 2003). The high-dip sinistral slip BF in the center and a suite of low-dip thrust faults at both sides

656 accommodate the oblique convergence caused by the Tarim Basin. BLTF = Beiluntai fault, NLTF = Nalati fault,

657 BF = Baoertu fault, JF = Junggar fault.

658 **Table 1** OSL sampling results for the Baoertu fault

659 **Table 2** Radiocarbon sampling results for the Baoertu fault

Figure 1.

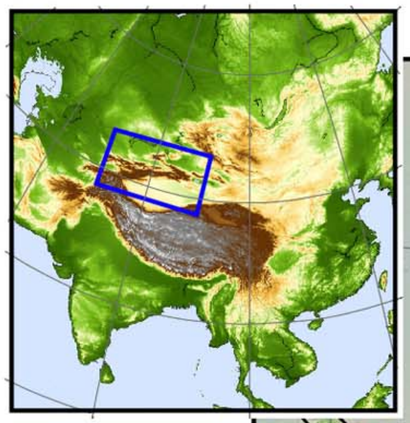

A

75°
80°
85°
90°
45°
40°

Kazakh Platform
Junggar Basin
Urumqi
Almaty
Bishkek
Fig. 1B
Fig. 10
Tian Shan
Tarim Basin
Pamir
200 km

Thrust fault
Strike-slip fault
Baoertu fault
Active fault
Pre-Cz Pre-Cenozoic
E Paleogene
N Neogene
Q Quaternary
Ms ≥ 8.0
7.0 ≤ Ms < 8.0
6.0 ≤ Ms < 7.0
5.0 ≤ Ms < 6.0

B

Q
Pre-Cz
N
E
Tian Shan
Bayanbulak Basin
Toksun
Turpan Basin
A-KF
Ms 5.0
Pre-Cz
BLTF
KDF
Hejing
Heshuo
Yanqi
Yanqi Basin
Kumish Basin
Bosten Lake
50 km

43°
42°
84°
85°
86°
87°
88°

Figure 2.

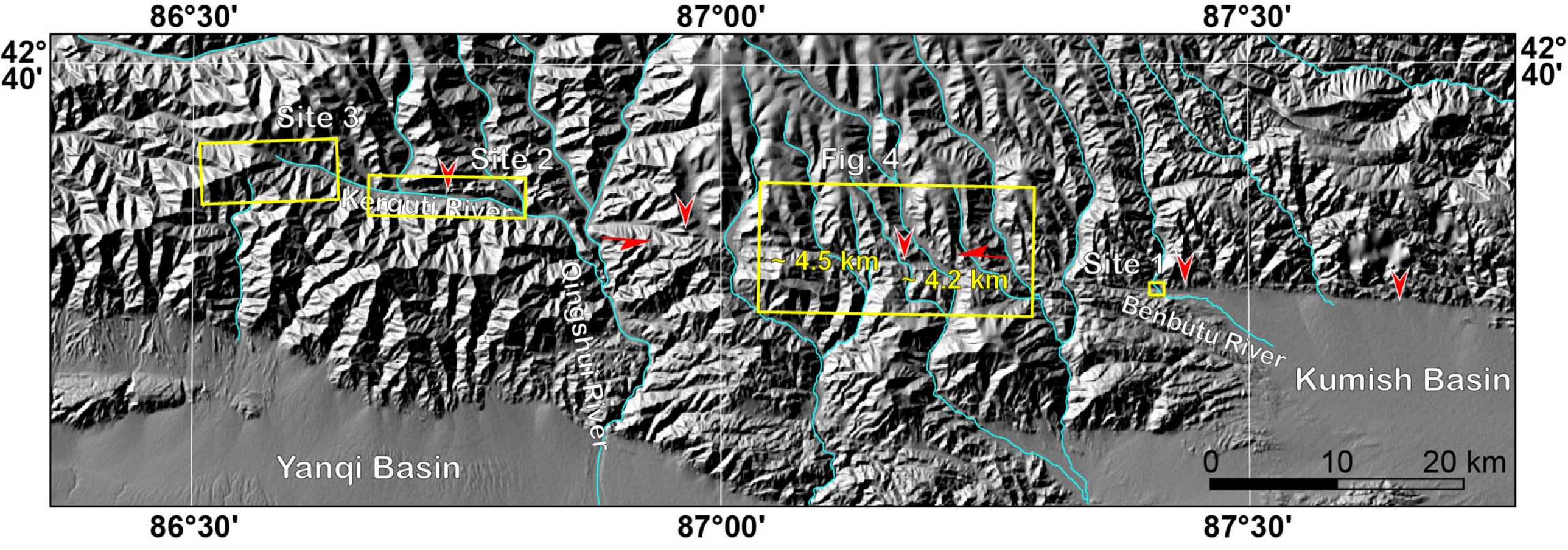
86°30'
87°00'
87°30'
42°
40'
Site 3
Site 2
Kerguti River
Fig. 4
~ 4.5 km
~ 4.2 km
Site 1
Benbutu River
Qingshuihe River
Yanqi Basin
Kumish Basin
0
10
20 km

Figure 3.

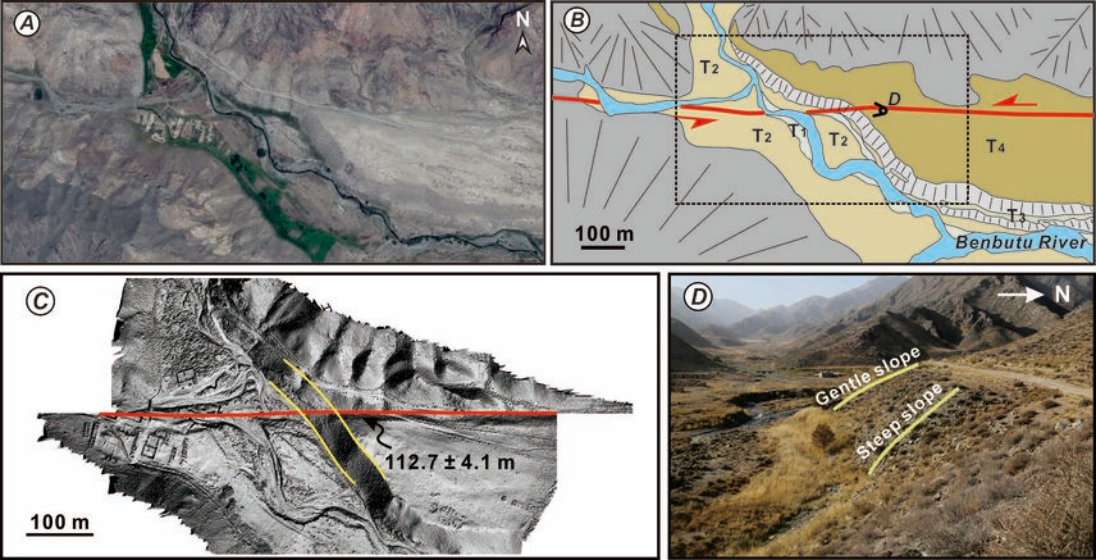
A
N
B
T2
T2
T1
T2
D
T4
T3
100 m
Benbutu River
C
112.7 ± 4.1 m
100 m
D
N
Gentle slope
Steep slope

Figure 4.

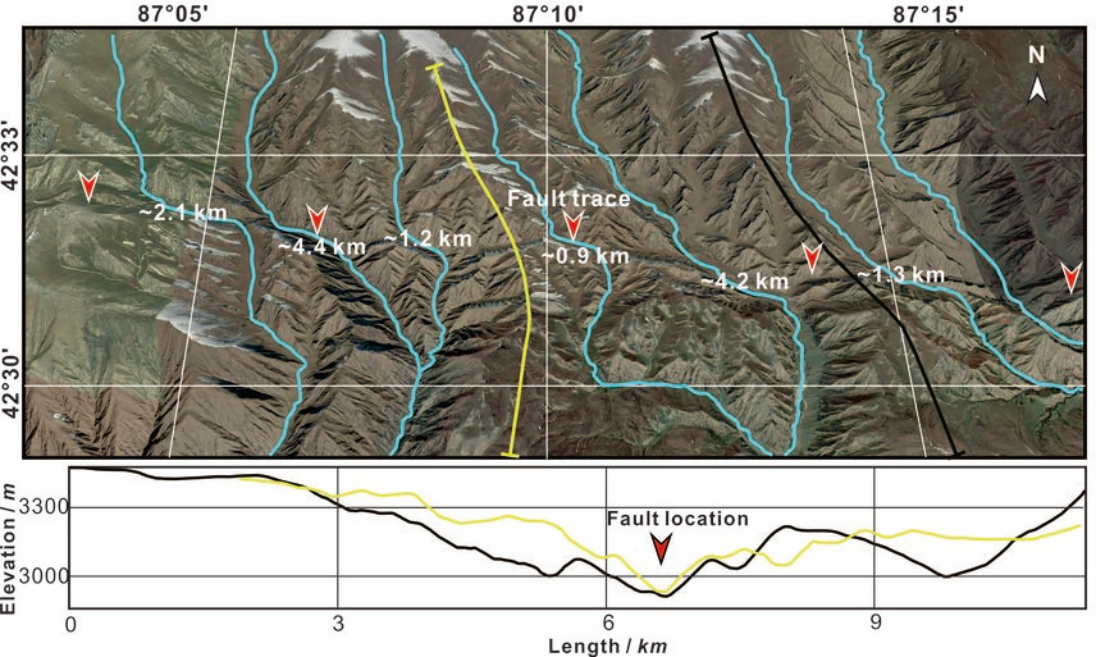
87°05'
87°10'
87°15'
42°33'
42°30'
N
~2.1 km
~4.4 km
~1.2 km
Fault trace
~0.9 km
~4.2 km
~1.3 km
Elevation / m
3300
3000
Fault location
0
3
6
9
Length / km

Figure 5.

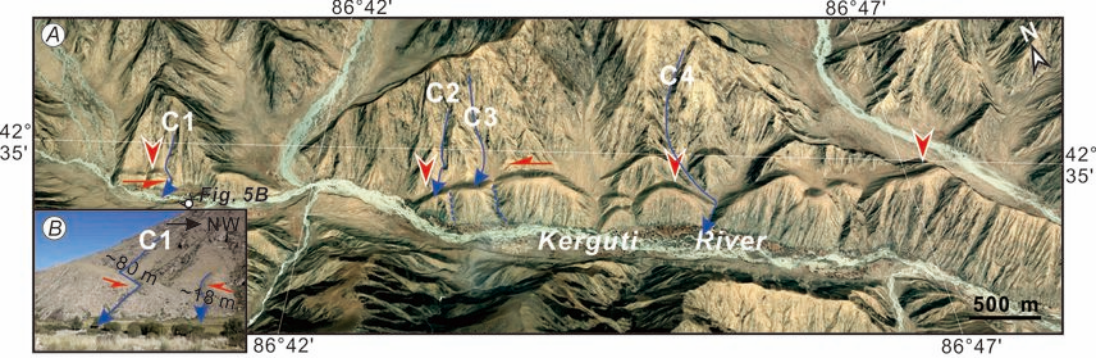
86°42'
86°47'
A
N
42°
35'
C1
C2
C3
C4
Fig. 5B
B
C1
NW
~80 m
~18 m
Kerguti River
500 m
86°42'
86°47'

Figure 6.

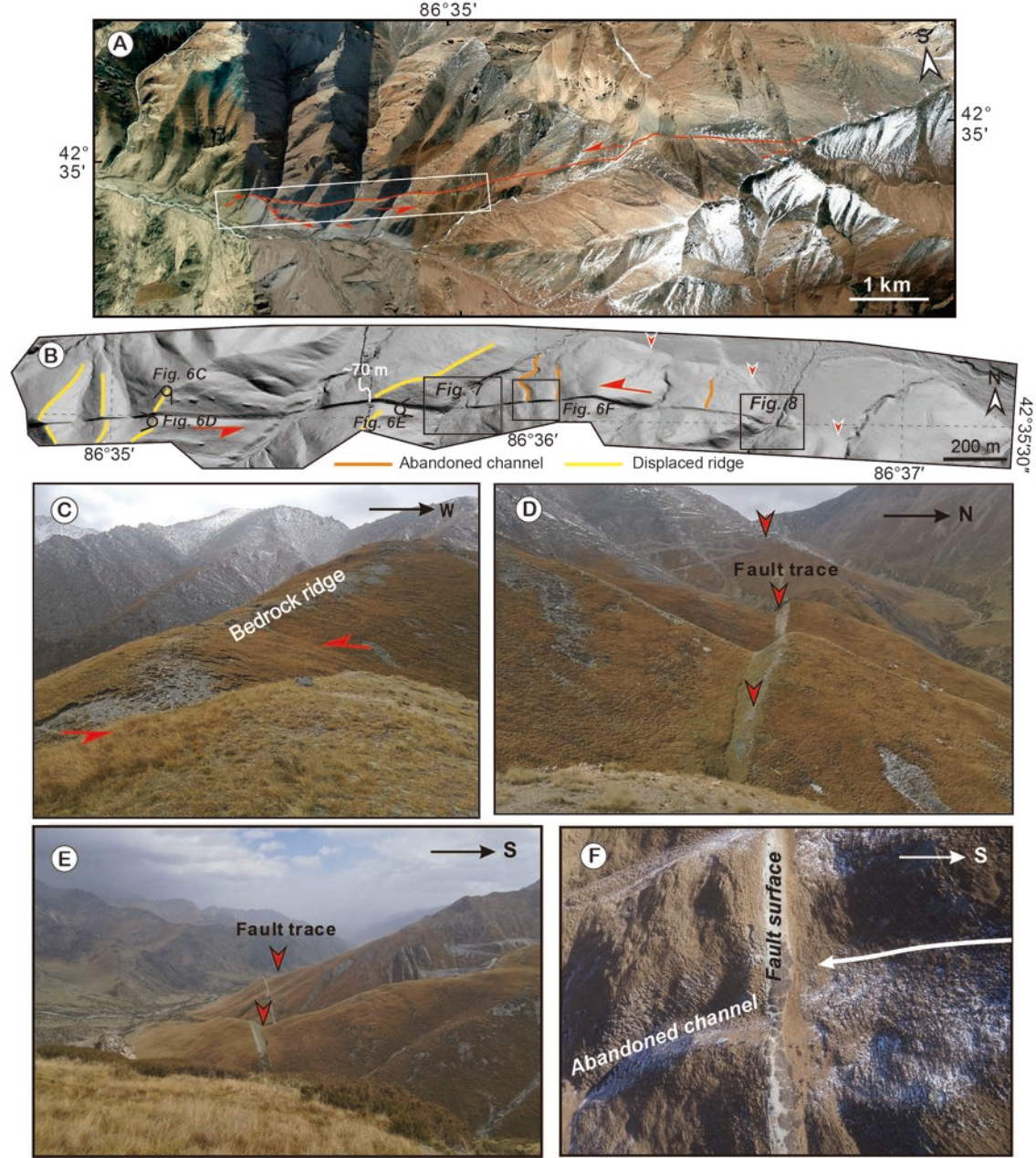
86°35′
A
42°
35′
1 km
B
Fig. 6C
Fig. 6D
~70 m
Fig. 6E
Fig. 7
Fig. 6F
Fig. 8
86°35′
86°36′
86°37′
42°35′30″
200 m
Abandoned channel
Displaced ridge
C
W
Bedrock ridge
D
N
Fault trace
E
S
Fault trace
F
S
Fault surface
Abandoned channel

Figure 7.

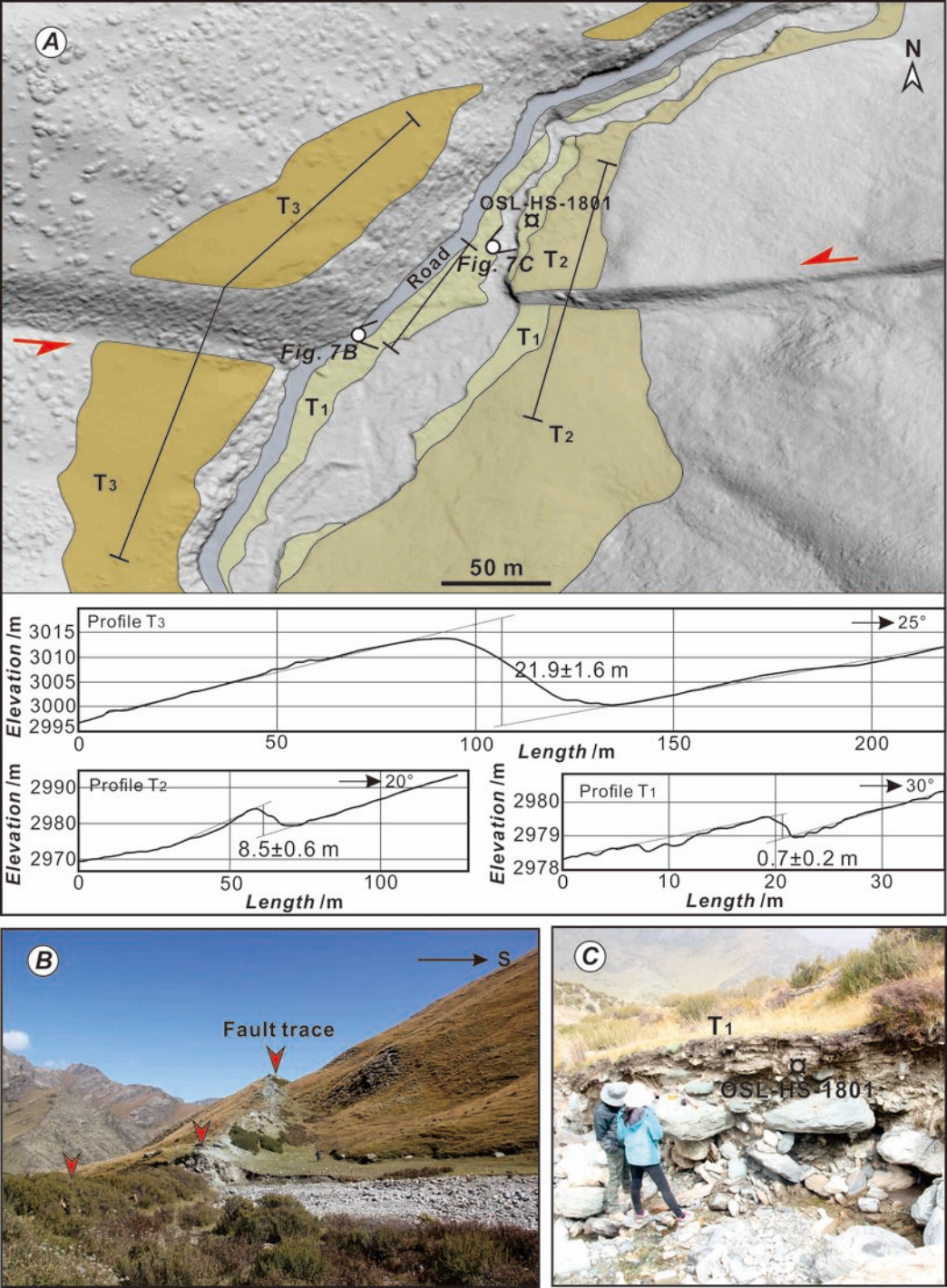
A
N
T3
T1
T2
OSL-HS-1801
Fig. 7C
Fig. 7B
Road
50 m
Profile T3
25°
21.9±1.6 m
Elevation /m
Length /m
Profile T2
20°
8.5±0.6 m
Profile T1
30°
0.7±0.2 m
B
S
Fault trace
C

Figure 8.

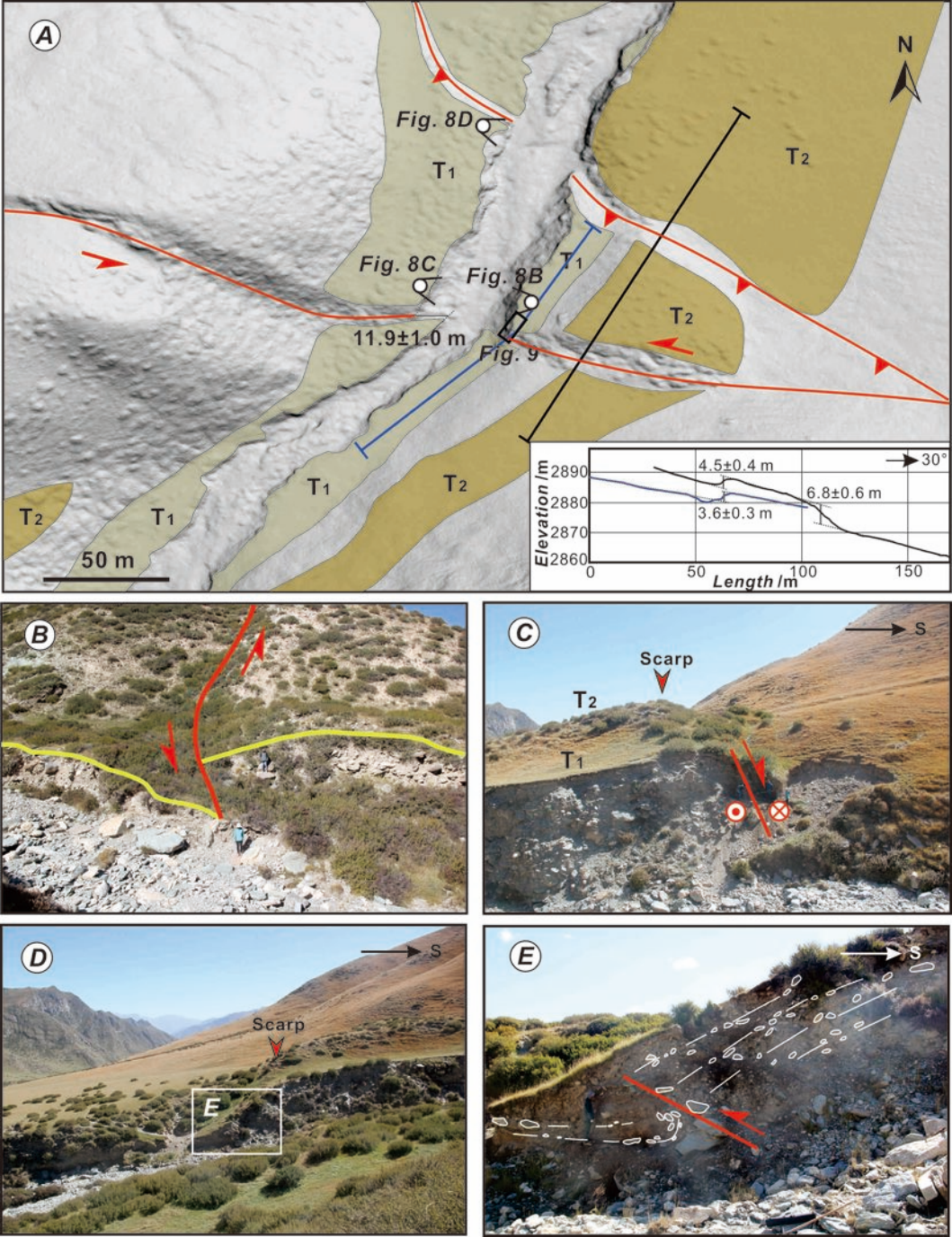
A
N
Fig. 8D
Fig. 8C
Fig. 8B
Fig. 9
T1
T2
11.9±1.0 m
50 m
4.5±0.4 m
6.8±0.6 m
3.6±0.3 m
30°
Elevation /m
2890
2880
2870
2860
0
50
100
150
Length /m
B
C
Scarp
S
D
E

Figure 9.

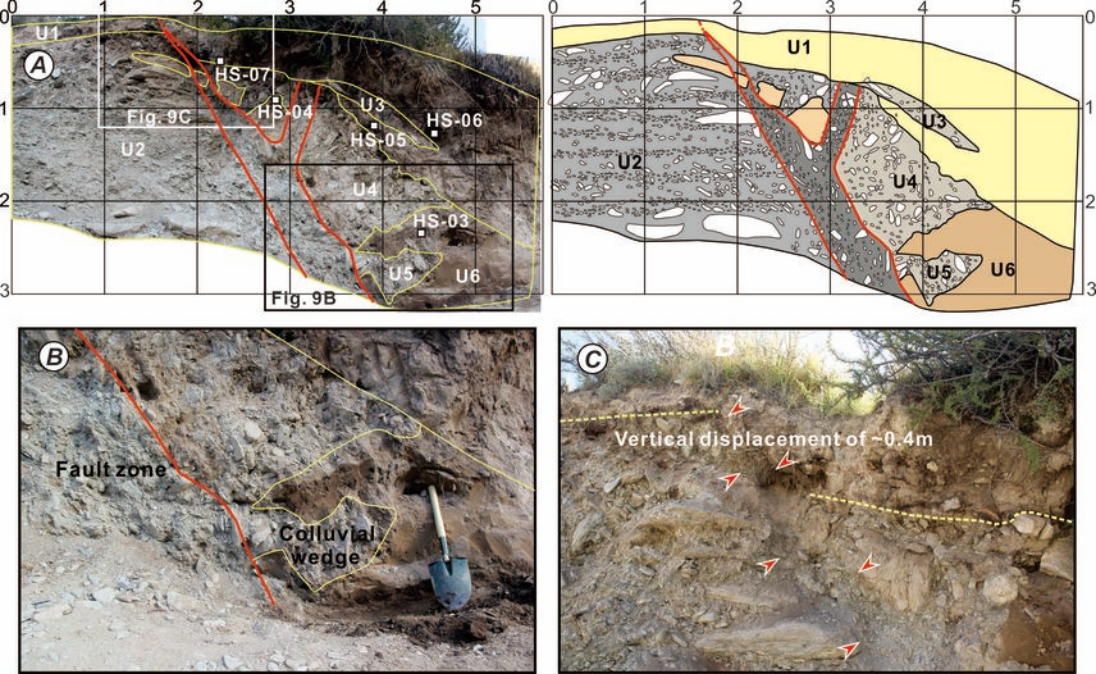
A
U1
HS-07
HS-04
U3
HS-06
HS-05
Fig. 9C
U2
U4
HS-03
U5
U6
Fig. 9B
U1
U3
U2
U4
U5
U6
B
Fault zone
Colluvial wedge
C
Vertical displacement of ~0.4m

Figure 10.

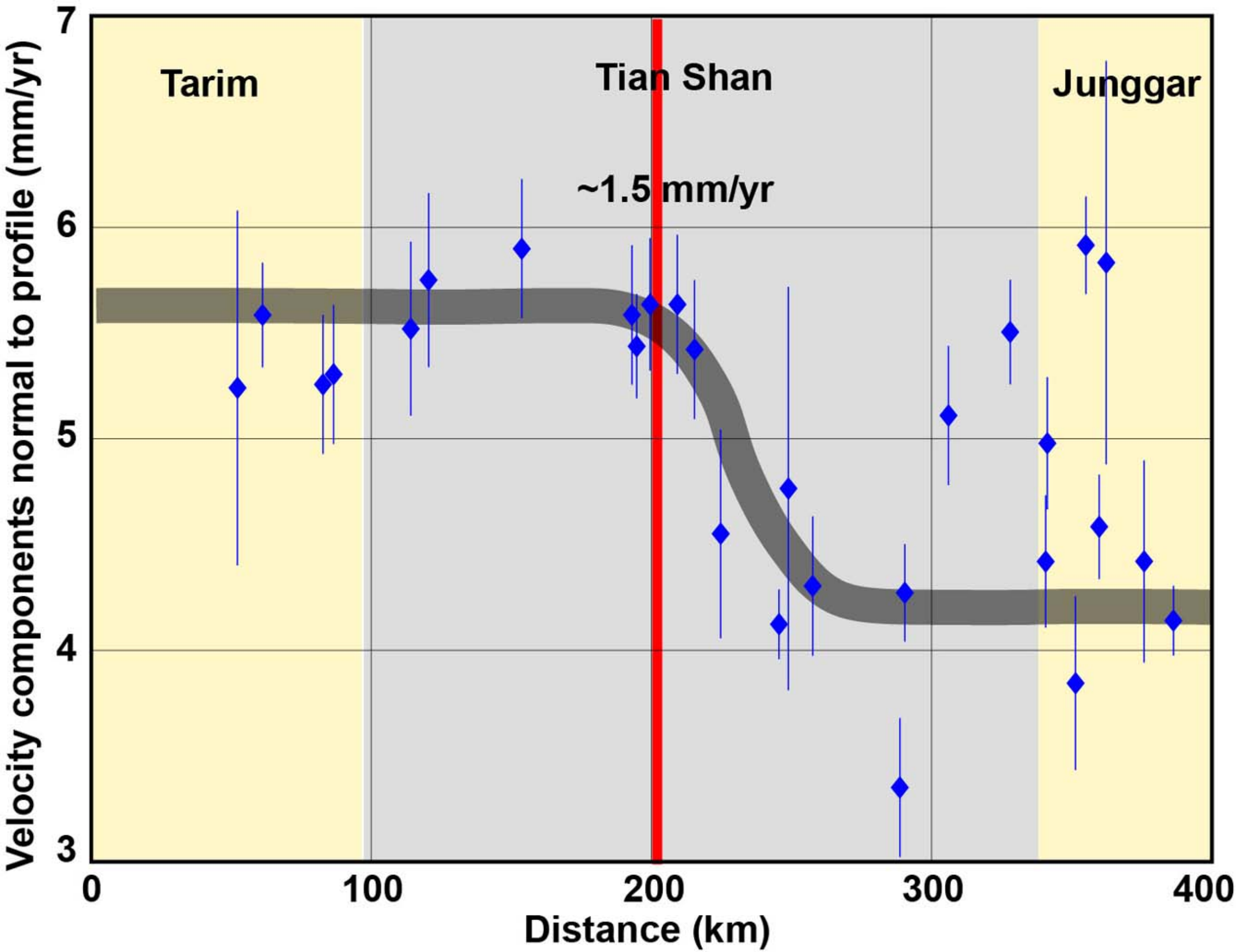
Tarim
Tian Shan
Junggar
~1.5 mm/yr
Velocity components normal to profile (mm/yr)
7
6
5
4
3
0
100
200
300
400
Distance (km)

Figure 11.

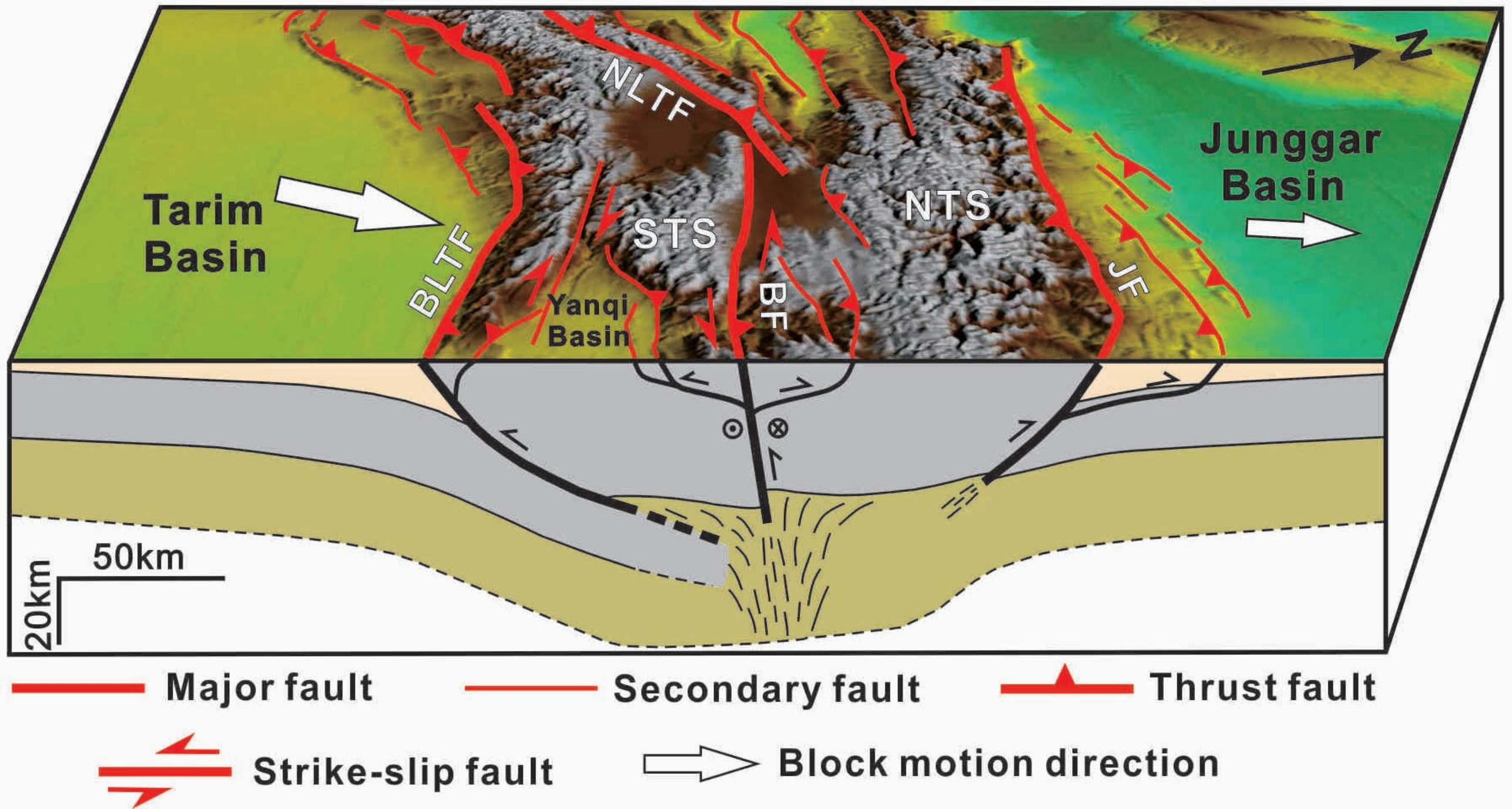
N
NLTF
Tarim
Basin
BLTF
STS
Yanqi
Basin
BF
NTS
JF
Junggar
Basin
50km
20km
Major fault
Secondary fault
Thrust fault
Strike-slip fault
Block motion direction

Table 1

Sample number	Sample site	Depth (m)	Moisture content	U-238 (Bg/Kg)	Th-232 (Bg/Kg)	K-40 (Bg/Kg)	Environmental dose rate (Gy/ka)	Equivalent dose amount (Gy)	OSL age (ka)
OSL-HS-1801	Upper layer of T_1 terrace	~0.35	5%	33.5±6.8	53.1±3.7	756.3±30.3	3.91±0.10	4.66±0.63	1.19±0.20

Table 2 [a]

Sample number	Laboratory number	Sample material	δ13C (%)	Conventional age [b]	Calibrated ages [c]	Probability area
HS-03	Beta-508446	Charcoal	-22.3	4460 ± 30 BP	5286-5158 cal BP	48.3%
					5090-4970 cal BP	36.4%
					5143-5098 cal BP	10.6%
HS-04	Beta-508447	Charcoal	-21.7	5970 ± 30 BP	6892-6730 cal BP	95.4%
HS-05	Beta-508448	Charcoal	-25.8	5340 ± 30 BP	6210-6001 cal BP	93%
					6263-6250 cal BP	2.4%
HS-06	Beta-508449	Organic sediment	-20.8	4400 ± 30 BP	5048-4866 cal BP	94.4%
					5211-5203 cal BP	1%
HS-07	Beta-508450	Charcoal	-23.9	4740 ± 30 BP	5584-5499 cal BP	75.3%
					5379-5328 cal BP	20.1%

[a] Reported ^{14}C ages used Libby half-life (5568 yr) and referenced to the year CE 1950. Our sample was tested by AMS at Beta Analystic.

[b] Analytical uncertainty is reported at 1σ.

[c] Probability method referencing Bronk Ramsey (2009); Calendar age calibrated using 2013 INTCAL program (Reimer et al., 2013). Associated age range reported at 2σ.